

Adaptive Capon beamforming for lensless electron cyclotron emission imaging with high spatial resolution

Idei, H.

Research Institute for Applied Mechanics, Kyushu University

Fukuyama, M.

Interdisciplinary Graduate School of Engineering Sciences, Kyushu University

Sakai, S.

Interdisciplinary Graduate School of Engineering Sciences, Kyushu University

Mishra, K.

Institute for Plasma Research

他

<https://hdl.handle.net/2324/7174490>



出版情報 : Review of Scientific Instruments. 93 (10), 2022-10-20. AIP Publishing
バージョン :
権利関係 :



RESEARCH ARTICLE | OCTOBER 20 2022

Adaptive Capon beamforming for lensless electron cyclotron emission imaging with high spatial resolution

Special Collection: [Proceedings of the 24th Topical Conference on High-Temperature Plasma Diagnostics](#)


H. Idei ; M. Fukuyama; S. Sakai; K. Mishra; K. Nishimura; R. Ikezoe ; T. Onchi; T. Ido ; K. Hanada




Rev. Sci. Instrum. 93, 103531 (2022)

<https://doi.org/10.1063/5.0101632>






Lock-in Amplifier



Zurich
Instruments

[Find out more](#)



Boxcar Averager

Boost Your Optics and Photonics Measurements

Adaptive Capon beamforming for lensless electron cyclotron emission imaging with high spatial resolution

Cite as: Rev. Sci. Instrum. 93, 103531 (2022); doi: 10.1063/5.0101632

Submitted: 2 June 2022 • Accepted: 20 September 2022 •

Published Online: 20 October 2022



H. Idei,^{1,a)} M. Fukuyama,² S. Sakai,² K. Mishra,³ K. Nishimura,⁴ R. Ikezoe,¹ T. Onchi,¹ T. Ido,¹ and K. Hanada¹

AFFILIATIONS

¹Research Institute for Applied Mechanics, Kyushu University, Kasuga 816-8560, Japan

²Interdisciplinary Graduate School of Engineering Sciences, Kyushu University, Kasuga 816-8580, Japan

³Institute for Plasma Research, Gandhinagar 382428, India

⁴Research Institute for Sustainable Humanosphere, Kyoto University, Uji 611-0011, Japan

Note: This paper is part of the Special Topic on Proceedings of the 24th Topical Conference on High-Temperature Plasma Diagnostics.

a) Author to whom correspondence should be addressed: idei@tri-am.kyushu-u.ac.jp

ABSTRACT

Electron cyclotron emission (ECE) imaging diagnostics incorporating a lensless approach have been developed for measurements involving active spatial selectivity and direction-of-arrival estimation. The Capon method for adaptive-array analysis was proposed to improve the spatial resolution of the two-dimensional ECE imaging technique. Broadband noise source emissions were used to simulate the ECE to verify the practical effectiveness of the Capon method in the ECE imaging. Multiple noise source emission positions were properly estimated with a high spatial resolution using the Capon method.

Published under an exclusive license by AIP Publishing. <https://doi.org/10.1063/5.0101632>

I. INTRODUCTION

Electron cyclotron emission (ECE) measurement is a popular diagnostic method for observing the electron temperature evolution in plasmas. The ECE from the energetic electron component may prevent proper measurement of the electron temperature evolution. Meanwhile, oblique ECE diagnostics have been developed to understand the acceleration mechanism of energetic electrons. An oblique ECE diagnostic was developed to probe the distorted electron momentum distribution function during the lower hybrid current drive on the PBX-M tokamak.¹ In the ASDEX tokamak, the two oblique ECE diagnostics were also developed for simultaneous measurements of electron streaming co- and counter-directionally with the plasma current in electron cyclotron (EC) heating and current drive (HCD),² which was used to measure the electron distribution function directly at the heating deposition site in the phase space. Fully non-inductive EC plasma ramp-up experiments have been conducted in the Q-shu university experiment with steady-state spherical tokamak (QUEST) with 8.2 and 28 GHz waves,^{3–5}

attaining the high plasma current (≤ 80 kA) through the effective creation of highly energetic electrons. Wide viewing involving active spatial selectivity in the co- and counter-directions is advantageous for observing the oblique ECE from plasmas with highly energetic electrons. The adaptive-array approach using a lensless technique has been attractive in terms of active spatial selectivity of observation.

ECE diagnostics suffer from a cutoff in which the wave cannot propagate in a high-density plasma. Conversely, the EC waves (ECWs) in the HCD cannot penetrate the high-density plasma beyond the cutoff. However, when the ECW approaches the cutoff from the low-magnetic field side at an optimal angle to the plasma, it converts into an electron Bernstein (EB) wave, which can propagate in the high-density plasma.⁶ EB wave HCD (EBWHCD) using the mode conversion is a potential candidate for the HCD scenario in the high-density plasma if the ECW can be injected into the narrow mode conversion window.⁷ EBWHCD experiments have been explored in the QUEST to sustain high-density plasma environments.⁸ As the EB emission (EBE) is measured

under the reversed process of EBWHCD, EBE diagnostics are useful for measuring the electron temperature in high-density plasmas⁹ and finding the narrow mode conversion window. An adaptive-array approach involving a lensless method was developed to find the mode conversion window in terms of the direction-of-arrival (DoA) estimation. In the MAST, the mode conversion windows were properly evaluated through the cross-correlation and inverse Fourier transform techniques, which were essentially equivalent to the beamforming method used in this study.^{10,11} In DoA estimation, proof-of-principle experiments using an emission source whose location was known beforehand were important for verifying the estimation. A broadband noise source (NS) was used to simulate the ECE or EBE, and a single NS emission was properly estimated in the beamforming adaptive-array analysis.^{12,13} In this study, a novel Capon method was first applied to confirm whether multiple sources could be accurately estimated at a high spatial resolution. The adaptive-array-analysis methods, including the Capon method, are comprehensively described in Ref. 14.

The remainder of this paper is organized as follows: Sec. II introduces the experimental apparatus and setup. Section III presents the detected signals of the NS emissions and an ECE in QUEST. Section IV describes the basic equations used in the adaptive-array analysis. Two-dimensional images analyzed for a single NS emission and multiple NS emissions are presented and discussed in Sec. V. Finally, the conclusions are presented in Sec. VI.

II. EXPERIMENTAL APPARATUS AND SETUP

Signals from the multiple-element antenna, as typified by the phase array antenna (PAA), were used in the adaptive-array analysis. A 4×4 PAA was developed for beam focusing and steering to conduct EBWHCD experiments with controlled launching at the QUEST.¹⁵ A 4×2 PAA fabricated as a prototype¹⁶ was used as the receiving antenna in this study. Figure 1 shows a photograph taken from the front side of the receiving port apertures of the 4×2 PAA. Labels 1–8 represented the port numbers of the 4×2 PAA. The side of the square waveguide port was 22.9 mm (0.90 in.) on the long side of the standard fundamental rectangular waveguide WR90. The wall thickness was 1.5 mm, and the wall was attached via T-type penetration welding using an electron beam. Broadband (0.7–18 GHz) NS emission was amplified and launched from a broadband (7.5–18 GHz) quad-ridged waveguide antenna to the 4×2 receiving PAA in the normal direction. The propagation distance between the launching and receiving antennae was 0.483 m.



FIG. 1. Photograph of a 4×2 phased array antenna (PAA) made of aluminum. Labels 1–8 show port numbers of the 4×2 PAA. PAA is used as a receiving antenna in this study.

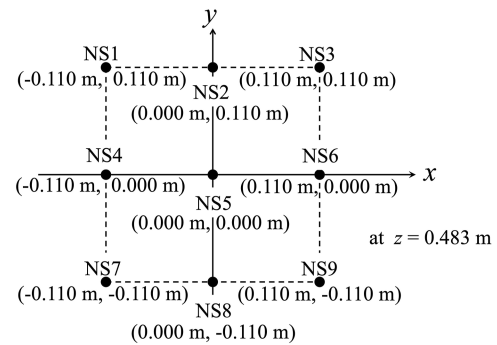


FIG. 2. Nine noise source position (NS1-9) coordinates in the x - y plane normal to the propagation onto the receiving PAA.

The launcher-waveguide side was small (\sim three-quarters of the measured wave wavelength); therefore, the emissions spread widely over the receiver ports along the propagation direction. Figure 2 shows nine NS positions scanned in the x - y plane normal to the propagation. The (x, y) coordinates of the observation were defined with respect to the origin of the port-array center at the 4×2 PAA when looking the NSs from the backside of the PAA. If the PAA is installed to a horizontal port facing to the center post in the QUEST, the x direction is equivalent to the toroidal direction. Major and minor radii are $R_0 \approx 0.64$ m and $R_a \approx 0.42$ m in the QUEST, respectively. The radial position of the PAA front aperture may be around 1.35 m. The maximum viewing oblique angle in the toroidal direction becomes 27.9° when observing the oblique ECE at R_0 , depending on the observation radius. The NS1, 3, 7, and 9 positions were nearest to ports 1, 4, 5, and 8 of the PAA shown in Fig. 1, respectively. In the DoA estimation for multiple NS positions, each NS emission was independently measured and then summed to obtain multiple NS emissions.

The single-sideband intermediate-frequency (IF) components of the NS emission were measured via heterodyne detection using a local synthesizer. The measured IF signals were filtered at 70 MHz bandpass filters with a 5 MHz (± 2.5 MHz) 3 dB bandwidth and amplified using low-noise amplifiers. In- and quadrature-phase (IQ) IF signals were detected with a data streaming of 1 MS/s after pre-processing using field-programmable gate array circuits at software-defined radios (SDRs) of universal software radio peripheral network devices (Ettus: N210). SDRs have been used for adaptive-array analyses on ECE radiometry and reflectometry in QUEST.^{13,17,18} The streaming IQ data size was significantly reduced from the streaming full data size without pre-processing. A 10 MHz rubidium standard clock was shared with the local synthesizer and SDRs for phase locking among the devices. The operating frequencies at the local synthesizer and the SDR were 8.57 GHz and 70 MHz, respectively, while emission signals of 8.5 GHz were detected in the proof-of-principle experiments. As the central magnetic field was 0.25 T in QUEST, the emission was in the range of fundamental ECE frequencies. A pulse-per-second signal was prepared for the synchronized operation of the SDRs. The two SDRs communicate using a multiple-input and multiple-output connection to share the 10 MHz clock and the pulse-per-second signal. The number of Ethernet connections can be reduced because the IQ

signals streamed to the PC from the two SDRs in a shared Ethernet master/slave mode under multiple-input and multiple-output connections.

The instrument sensitivities and phase offsets at the ports were calibrated based on the field evolution in front of the port apertures along the propagation.^{12,13} Another synthesizer under phase-locking was used to launch a probing wave onto the receiving PAA. In addition, the reference field signal was measured before launching to normalize the received amplitude and determine the phase difference between the launching and receiving phases. The field amplitude and phase evolution were fitted as $1/z$ and kz dependences to evaluate the sensitivity and phase offsets, respectively. Here, k is the wavenumber of the measuring frequency, 8.5 GHz. The evaluated sensitivities and phase offsets were used to calibrate the detected signals before adaptive-array analyses.

The ECE in the QUEST experiments was measured using a single-sideband mixer, waveguide antenna, and SDR at a sampling rate of 1 MS/s for the heterodyne detection. A local synthesizer was used under the phase locking with the SDR. The synthesizer and SDR frequencies were set as 13.07 and 70 MHz, respectively, and the 13 GHz IQ signals of the ECE were detected.

III. EXPERIMENTAL RESULTS

Figure 3 shows time evolution of the IQ signals of the NS emission measured at the output of the SDR with the sampling rate of 1 MS/s. The measured IQ signals highly fluctuated. The broadband emissions with the 5 MHz bandwidth around the 70 MHz IF frequency were numerically sampled, down-converted, and decimated to the rate of 1 MS/s at the SDR, thereby causing aliasing by five times. In Ref. 13, the fluctuating signals were analyzed by a fast Fourier transform (FFT), and all the frequency components were averaged. A stable amplitude evolution was obtained by the averaging among the frequency components, whereas the phase evolution was still random. However, the phase differences among the ports were stable in the evolution even with the aliasing, depending on the differences of the arrival distances to the ports. Thereafter, a single NS emission point was fairly estimated in the adaptive-array analysis, whereas there were growing concerns whether multiple emission sources could be properly analyzed in the DoA estimation.

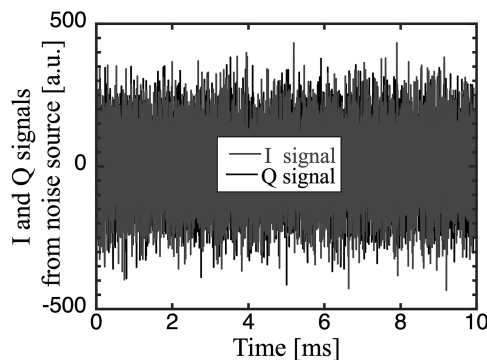


FIG. 3. Time evolution of in-(I) and quadrature-(Q) phase signals from the noise source (NS) emission detected at a sampling rate of 1 MS/s.

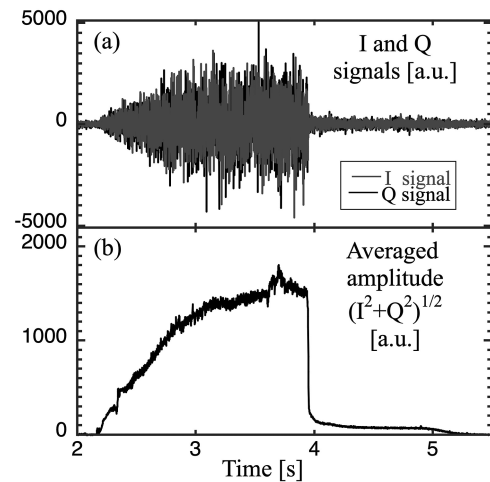


FIG. 4. Time evolution of (a) IQ signals of electron cyclotron emission in the QUEST and (b) their averaged amplitude over 1024 samples at a sampling rate of 1 MS/s.

In this study, the correlation matrix composed of sample-averaged elements of complex products with measured signals that have not been processed by an FFT is introduced in Sec. IV. The aliasing does not affect essentially the adaptive-array analysis of Sec. IV because of the incoherency of the emission by which the cross-correlations between the different spectral segments become zero, whereas all the element values of the correlation matrix quintuple. The 1024 sampled signals were used to evaluate the correlation matrix.

Figure 4 shows the time evolution of the IQ signals and their averaged ECE amplitude in the non-inductive EC plasma ramp-up experiments with the 28 GHz wave on the QUEST. The ECE IQ signals were also measured at a sampling rate of 1 MS/s, and their amplitudes were averaged over 1024 samples. The IQ signals fluctuated, whereas the smooth time evolution of the amplitude was evaluated after averaging, as often measured using normal ECE radiometers. The bandwidth at the IF filter and the sampling rate at the SDR will be narrower and higher to avoid the aliasing, respectively.

In this study, multiple NS emissions with fluctuating IQ signals were used to simulate the ECE in the imaging.

IV. BASIC EQUATIONS IN ADAPTIVE ARRAY ANALYSIS

In the adaptive-array analysis using multiple n elements, the measured complex time evolution, $x_i(t)$ [$i = 1, \dots, n$], was summed up with the complex weight w_i [$i = 1, \dots, n$] to evaluate the complex output of $y(t) = \sum_{i=1}^n w_i^* x_i(t)$. Here, $*$ is a complex conjugate operator. The complex measured signals, $x_i(t)$, are expressed as $x_i(t) = x_{Ii}(t) + ix_{Qi}(t)$, where $x_{Ii}(t)$ and $x_{Qi}(t)$ are the I and Q signals sampled at the SDR, respectively. In the vector form, $y(t) = \mathbf{W}^H \mathbf{X}(t)$ with a weight vector \mathbf{W} and an array-input vector of the measured signals $\mathbf{X}(t)$, where $\mathbf{W} = [w_1, \dots, w_n]^T$ and $\mathbf{X}(t) = [x_1(t), \dots, x_n(t)]^T$. Here, H and T are the Hermitian conjugate and transpose operators, respectively. The weight vector of the

beamforming method, \mathbf{W}_{BF} , is expressed as a mode vector $\mathbf{a}(\theta, \phi)$ that shows a phase-delay array at the PAA port,

$$\mathbf{W}_{\text{BF}} = \mathbf{a}(\theta, \phi). \quad (1)$$

The zenith and azimuth angles, θ and ϕ , were defined as $\theta = \arctan(\sqrt{x^2 + y^2}/z)$ and $\phi = \arctan(y/x)$, respectively, with the (x, y) coordinates shown in Fig. 2 at a propagation distance of $z = 0.483$ m. The i th element of the mode-vector $a_i(\theta, \phi)$ is described as

$$a_i(\theta, \phi) = -k(dx_i \cos \phi \sin \theta + dy_i \sin \phi \sin \theta), \quad (2)$$

where dx_i and dy_i are the (x, y) coordinates of the i th port positions in Fig. 2. The phase delay of $\mathbf{a}(\theta, \phi)$ was evaluated along the path of the plane-wave analysis.

In Ref. 13, the output power $|y|^2$ was evaluated by using $\mathbf{a}(\theta, \phi)$ and signals X after averaging through an FFT. In this study, the average output power $P_{\text{out}} = E[|y(t)|^2]$ was evaluated using the correlation matrix R_{xx} as follows:

$$P_{\text{out}} = \mathbf{W}^H R_{xx} \mathbf{W} / 2, \quad (3)$$

where R_{xx} is expressed as

$$R_{xx} = E[\mathbf{X}(t)\mathbf{X}^H(t)] = \begin{bmatrix} E[x_1(t)x_1^*(t)] & E[x_1(t)x_2^*(t)] & \cdots & E[x_1(t)x_n^*(t)] \\ E[x_2(t)x_1^*(t)] & E[x_2(t)x_2^*(t)] & \cdots & E[x_2(t)x_n^*(t)] \\ \vdots & \vdots & \ddots & \vdots \\ E[x_n(t)x_1^*(t)] & E[x_n(t)x_2^*(t)] & \cdots & E[x_n(t)x_n^*(t)] \end{bmatrix}, \quad (4)$$

where $E[\cdots]$ is the sample- or time-averaging operator.

In the Capon method,¹⁹ an attempt is made to turn a main receiving lobe into a specific observation direction in concert with the minimization of the contribution from the other direction in the DoA estimation. The Capon method has been used in a variety of measurements including a wide range of radio applications. One such example with respect to very-high-frequency radar is the high-resolution Capon imaging of atmospheric turbulence scatter.²⁰ The weight of the Capon method, \mathbf{W}_{CP} , can be evaluated using $\mathbf{a}(\theta, \phi)$ in Eq. (2) and the correlation matrix R_{xx} in Eq. (4) as follows:

$$\mathbf{W}_{\text{CP}} = \frac{R_{xx}^{-1} \mathbf{a}(\theta, \phi)}{\mathbf{a}(\theta, \phi)^H R_{xx}^{-1} \mathbf{a}(\theta, \phi)}.$$

The P_{out} distributions of multiple NS emissions were evaluated using \mathbf{W}_{BF} , \mathbf{W}_{CP} , and R_{xx} from Eq. (3) for the adaptive beamforming and Capon approaches.

V. RESULTS AND DISCUSSION

The spatial resolution of the adaptive-array analysis using the Capon method was tested using a single NS1 emission. The NS1-9 labels in Fig. 2 were used in this section. Figure 5 shows the P_{out} distributions of the NS1 emission analyzed using the beamforming and Capon methods. The measured 1024 samples of

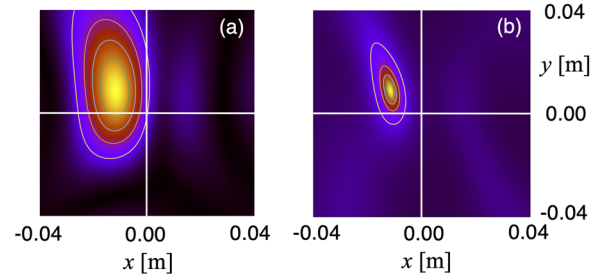


FIG. 5. Two-dimensional estimated power distributions P_{out} of a single NS1 emission analyzed using (a) beamforming and (b) Capon methods. The NS1 position is illustrated in Fig. 2.

the IQ signal were used to evaluate R_{xx} . The distributions were normalized by the maximum value of P_{out} . The distribution that appeared to be very similar to that in Ref. 13 was obtained from the beamforming analysis using a correlation matrix. The P_{out} peak-positions were $[(-0.114 \pm 0.0001) \text{ m}, (0.0891 \pm 0.0002) \text{ m}]$ and $[(-0.115 \pm 0.0006) \text{ m}, (0.0924 \pm 0.0020) \text{ m}]$ using the beamforming and Capon methods, respectively, where nine P_{out} distributions with 9216 (9×1024) samples were used to evaluate the averages and the standard deviations. The peak detection with the Capon method was more accurate with respect to the y direction, whereas the misalignment in the y direction as also noted in Ref. 13 is pointed out below. The spatial resolution was significantly improved using the Capon method for the DoA estimation of a single NS1 emission.

Figure 6 shows the P_{out} distributions of the two NS emissions from the NS1 and NS2 positions and from the NS1 and NS9 positions analyzed using the beamforming and Capon methods. The two NS1 and NS2 emission sources lying side-by-side could not be distinguished using the beamforming method; however, the Capon method properly distinguished the two emissions. Two distant NS1 and NS9 emission sources could be distinguished, even with the beamforming method. Furthermore, the spatial resolution was improved using the Capon method.

The P_{out} distributions of three NS emissions analyzed using the beamforming and Capon methods are shown in Fig. 7. The three NS emissions from the NS4, NS5, and NS6 positions were estimated as a zonal image horizontally elongated along the x -axis using the Capon method. In a precise sense, the zonal image was not located on the x -axis, whereas the NSs were set on the axis because of the misalignment in the experimental setup. The three NS1, NS5, and NS9 emissions were estimated as a zonal image in the second and fourth quadrants using the Capon method. The adaptive Capon analysis was highly effective for high-spatial DoA estimations, even with multiple NS emissions.

Vertically aligned NS emissions (e.g., NS1, NS4, and NS7 emissions) were also analyzed using the Capon method. The vertically elongated P_{out} distributions were evaluated with high spatial resolution in the x directions; however, significant spatial resolution was not attained in the y direction because of the small number of vertical elements in the 4×2 PAA receiving antenna.

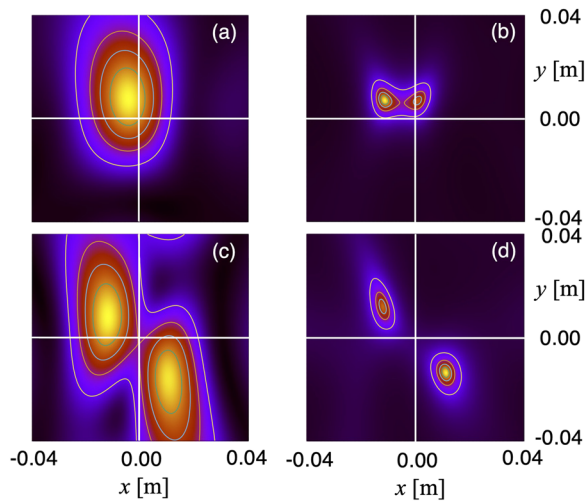


FIG. 6. Two-dimensional P_{out} distributions of the NS1 and NS2 emissions analyzed using (a) beamforming and (b) Capon methods. Figures (c) and (d) show the distributions of the NS1 and NS9 emissions involving the beamforming and Capon methods, respectively. The positions of the NS emissions are illustrated in Fig. 2.

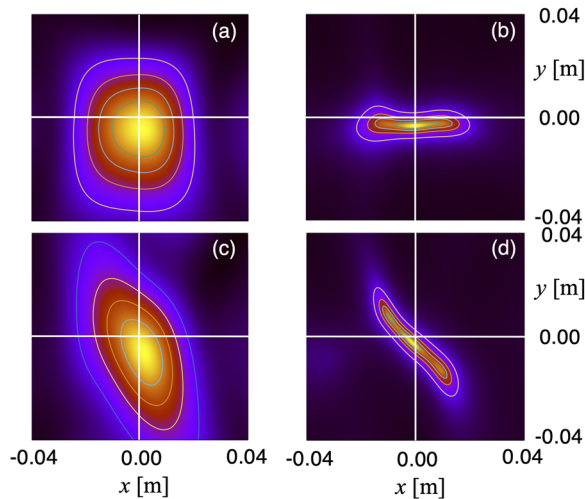


FIG. 7. Two-dimensional P_{out} distributions of the NS4, NS5, and NS6 emissions analyzed using (a) beamforming and (b) Capon methods. Figures (c) and (d) show the distributions of the NS1, NS5, and NS9 emissions involving the beamforming and Capon methods. The positions of the NS emissions are illustrated in Fig. 2.

VI. CONCLUSIONS

For lensless ECE imaging with a high spatial resolution, a novel Capon method was applied to proof-of-principle experiments involving multiple noise source emissions whose locations were known beforehand. In the direction-of-arrival estimation of a single noise source emission, a significant improvement in the spatial resolution was confirmed using the Capon method. Furthermore, two side-by-side noise source emissions that could not be distinguished

using a typical beamforming approach were detected. Three noise source emission positions were properly estimated as zonal images with the high spatial resolution. The Capon method is a powerful technique for the lensless ECE imaging diagnostics in terms of the active spatial selectivity and the direction-of-arrival estimation.

ACKNOWLEDGMENTS

This work was partially performed under the auspices and support of the NIFS Collaboration Research Program (Grant Nos. NIFS19KUTR136 and NIFS22KUTR169). This research study was partially supported by a Grant-in-Aid for Scientific Research (B) (JSPS KAKENHI Grant No. JP21H01067).

AUTHOR DECLARATIONS

Conflict of Interest

The authors have no conflicts to disclose.

Author Contributions

H. Idei: Conceptualization (lead); Data curation (lead); Formal analysis (lead); Funding acquisition (lead); Investigation (lead); Methodology (supporting); Software (lead); Writing – original draft (lead); Writing – review & editing (lead). **M. Fukuyama:** Data curation (supporting); Investigation (supporting); Software (supporting); Writing – original draft (supporting). **S. Sakai:** Data curation (supporting); Writing – original draft (supporting). **K. Mishra:** Conceptualization (supporting); Data curation (supporting); Formal analysis (supporting); Investigation (supporting); Writing – original draft (supporting); Writing – review & editing (supporting). **K. Nishimura:** Conceptualization (supporting); Methodology (lead); Writing – original draft (supporting). **R. Ikezoe:** Conceptualization (supporting); Writing – original draft (supporting); Writing – review & editing (supporting). **T. Onchi:** Conceptualization (supporting); Writing – original draft (supporting); Writing – review & editing (supporting). **T. Ido:** Conceptualization (supporting); Funding acquisition (supporting); Writing – original draft (supporting). **K. Hanada:** Conceptualization (supporting); Funding acquisition (supporting); Writing – original draft (supporting).

DATA AVAILABILITY

The data that support the findings of this study are available from the corresponding author upon reasonable request.

REFERENCES

- S. Preische *et al.*, *Rev. Sci. Instrum.* **68**, 409–414 (1997).
- S. S. Denk *et al.*, *Plasma Phys. Controlled Fusion* **63**, 015003 (2021).
- H. Idei *et al.*, *Nucl. Fusion* **57**, 126045 (2017).
- H. Idei *et al.*, *Nucl. Fusion* **60**, 016030 (2020).
- T. Onchi *et al.*, *Phys. Plasmas* **28**, 022505 (2021).
- J. Preinhaelter and V. Kopecký, *J. Plasma Phys.* **10**, 1 (1973).
- H. P. Laqua *et al.*, *Phys. Rev. Lett.* **90**, 075003 (2003).
- H. Idei *et al.*, *J. Plasma Fusion Res.* **9**, 2402112 (2010).

- ⁹F. Volpe and H. P. Laqua, *Rev. Sci. Instrum.* **74**, 1409 (2003).
- ¹⁰V. F. Shevchenko *et al.*, *J. Instrum.* **7**, P10016 (2012).
- ¹¹S. J. Freethy *et al.*, *Plasma Phys. Controlled Fusion* **55**, 124010 (2013).
- ¹²K. Mishura *et al.*, *Rev. Sci. Instrum.* **85**, 11E808 (2014).
- ¹³H. Idei *et al.*, *J. Instrum.* **11**, C04010 (2016).
- ¹⁴H. L. Van Trees, *Optimum Array Processing: Part IV of Detection, Estimation, and Modulation Theory* (John Wiley & Sons, 2004).
- ¹⁵H. Idei *et al.*, *AIP Conf. Proc.* **1406**, 473 (2011).
- ¹⁶H. Idei *et al.*, *IEEEJ Trans. Fundam. Mater.* **132**, 511 (2012).
- ¹⁷H. Idei *et al.*, *Rev. Sci. Instrum.* **85**, 11D842 (2014).
- ¹⁸H. Idei *et al.*, *J. Instrum.* **11**, C010140 (2016).
- ¹⁹J. Capon, *Proc. IEEE* **57**, 1408 (1969).
- ²⁰R. D. Palmer *et al.*, *Radio Sci.* **33**, 1585, <https://doi.org/10.1029/98rs02200> (1998).